Journal of The Electrochemical Society, 162 (4) C140-C149 (2015)

This manuscript has been authored by UT-Battelle, LLC under Contract No. DE-AC05-00OR22725 with the U.S. Department of Energy. The United States Government retains and the publisher, by accepting the article for publication, acknowledges that the United States Government retains a non-exclusive, paid-up, irrevocable, world-wide license to publish or reproduce the published form of this manuscript, or allow others to do so, for United States Government purposes. The Department of Energy will provide public access to these results of federally sponsored research in accordance with the DOE Public Access Plan (http://energy.gov/downloads/doe-public-access-plan).

Film Breakdown and Nano-Porous $Mg(OH)_2$ Formation from Corrosion of Magnesium Alloys in Salt Solutions

[a]M.P. Brady, [a]G. Rother, [a]L.M. Anovitz, [a]K.C. Littrell, [a]K.A. Unocic, [a,b]H.H. Elsentriecy, [a]G.-L. Song, [a]J.K. Thomson, [a]N.C. Gallego, [c]B. Davis

[a]Oak Ridge National Laboratory, Oak Ridge, TN USA

[b]Central Metallurgical Research & Development Institute, Cairo, Egypt

[c]Magnesium Elektron North America, Madison, IL USA

Contact: bradymp@ornl.gov

Abstract

Small angle neutron scattering (SANS) and scanning transmission electron microscopy (STEM) were used to study film formation by magnesium alloys AZ31B (Mg-3Al-1Zn base) and ZE10A (Elektron®717, E717: Mg-1Zn + Nd, Zr) in H_2O and D_2O with and without 1 or 5 wt.% NaCl. No SANS scattering changes were observed after 24 h D_2O or H_2O exposures compared with as-received (unreacted) alloy, consistent with relatively dense MgO-base film formation. However, exposure to 5 wt.% NaCl resulted in accelerated corrosion, with resultant SANS scattering changes detected. The SANS data indicated both particle and rough surface (internal and external) scattering, but with no preferential size features. The films formed in 5 wt.% NaCl consisted of a thin, inner MgO-base layer, and a nano-porous and filamentous $Mg(OH)_2$ outer region tens of microns thick. Chlorine was detected extending to the inner MgO-base film region, with segregation of select alloying elements also observed in the inner MgO, but not the outer $Mg(OH)_2$. Modeling of the SANS data suggested that the outer $Mg(OH)_2$ films had very high surface areas, consistent with loss of film protectiveness. Implications for the NaCl corrosion mechanism, and the potential utility of SANS for Mg corrosion, are discussed.

Introduction

Magnesium and its alloys are of great interest for a wide range of structural and functional applications, including lightweight automotive and aircraft structural materials, biomedical implants, fuel cells and hydrogen storage, batteries, etc. [1-7]. However, the high reactivity and rapid corrosion of Mg in many aqueous and humid environments is a key issue [8-11]. Of particular challenge and interest is the acceleration of Mg corrosion in the presence of salt species. Mechanisms of accelerated attack in salt solutions include enhanced local micro-galvanic coupling at alloy second phases and/or impurities (e.g. Fe, Ni, Cu etc.) and disruption of the MgO and/or $Mg(OH)_2$ base surface films by Cl- [3, 9, 12-26]. Film formation by Mg alloys under aqueous conditions can be quite complex, involving MgO, $Mg(OH)_2$, and $MgCO_3$ base phases, as well as complexes of those phases when alloy additions (e.g. Al) or environmental species (e.g. Cl-) become incorporated into parts or all of the film structure [15-17, 21, 27-34]. In some cases, porous and even filiform-like corrosion films have been reported on bare or surface-modified Mg alloys [11, 14, 16,18, 24, 35-38].

Small angle neutron scattering (SANS) has emerged as a powerful technique to assess structural and morphological features in the ~1 to up to ~200-300 nm feature size range (specific range accessed depends on the instrument capabilities and settings, as well as the nature of neutron scattering from the test samples) [39, 40]. Information can be obtained regarding size, morphology, and number density of scatterers (e.g. 2nd phase precipitates, phase separation, grain structure, voids, pores, etc.), as well as surface area and roughness [e.g. 7, 41-43]. Small angle neutron scattering can also be used to gain insights into the incorporation of light elements such as H into structures, including the potential to use isotopic labeling contrast with species such as D, as well as magnetic moments. To date, SANS has not been widely applied to alloy oxidation and corrosion phenomena [e.g. 42, 43], and no papers applying it to corrosion of Mg alloys could be located. A key advantage of SANS for corrosion phenomena is the ability to obtain data over an entire sample volume due the penetrating power of neutrons, including the potential for in-situ study. A more detailed description of the SANS technique is provided in Appendix A.

The goal of the present work was to apply advanced characterization techniques to better understand the nano and microstructure features of aqueous film formation by Mg alloys in the presence of NaCl. Of particular interest was evaluation of the potential utility of SANS coupled with cross-section scanning transmission electron microscopy (STEM) to provide new insights into the corrosion films formed by Mg. The corrosion products formed on two commercial Mg alloys after exposure in H_2O or D_2O with and without 5 wt.% NaCl was assessed by SANS and STEM. Films formed in 5 wt.% NaCl solutions, particularly when D_2O was used, were found to result in significant changes in SANS data that were correlated with the formation of thick, nanoporous $Mg(OH)_2$ films.

Experimental

Two commercial Mg alloys representative of the major Mg-Al-Zn class and rare-earth and Zr modified class of Mg alloys were selected for study: AZ31B (Mg-3Al-1Zn base, H24 temper, "half hard" strain hardened) and Elektron® 717 (ZE10A type alloy of Mg-1Zn + Nd/Zr, F temper, as-fabricated, referred to in this paper as E717 for convenience). The alloy test samples were electro-discharged machine (EDM) cut from wrought coil sheet ~1.5 to 1.6 mm thick obtained from Magnesium Elektron North America (MENA), Madison, IL USA. The E717 alloy has recently been shown to be amenable to formation of door panels by warm forming techniques, making it of particular interest to automotive applications [44]. Analyzed compositions are shown in Table 1. The AZ31B and E717 sheet material was used for SANS study as nominal ~25 mm x 25 mm x 1.5 mm rectangular test samples prepared to a 1200 grit surface finish wet ground with SiC paper, cleaned with acetone and deionized water, and dried with an air stream. Samples were then stored in a desiccator for at least 24 h prior to the corrosion exposures.

The corrosion exposures for ex-situ SANS and cross-section STEM study were conducted by immersion for 24 h in a plastic beaker with loosely fitted lid, filled with 10 ml of D_2O, H_2O, D_2O + 5 wt.% NaCl, and H_2O + 5 wt.% NaCl. The D_2O was obtained as 99.96 at.% isotope purity from Cambridge Isotope Laboratories, Inc., Andover, MA USA. The H_2O was high purity deionized water, trade name OmniSolv® Water from VWR, Radnor, PA USA. One edge of the

test sample face was lifted to permit ready access of the test solution to both major faces of the test samples.

To gain further insight into the effects of NaCl on early stage film formation, an additional set of AZ31B and E717 test samples was also studied by TEM. This material was EDM cut as test samples ~9 mm in diameter and ~1 to 1.5mm thick from AZ31B and E717 plate material of similar composition, but different materials batches, to the sheet material used for SANS study (Table 1). Exposures were conducted for 4 h in 5 ml of H_2O + 1 wt.% NaCl in an attempt to capture the earlier stages of film growth effects by NaCl. The alloy test samples were EDM cut from the same AZ31B and E717 batches as used in our recent TEM study [32] of film formation by these alloys in pure deionized water (no NaCl additions), with a 1200 grit surface finish and the same preparation methodology as with the SANS test samples and earlier TEM work.

Small-angle neutron scattering measurements were performed at the General Purpose SANS (CG2) instrument at Oak Ridge National Laboratory's High Flux Isotope Reactor (HFIR) facility. The neutron wavelength was 4.75 Å, with a wavelength distribution $\Delta\lambda / \lambda = 0.15$. A sample aperture of 8 mm and sample-to-detector distances of 2 m and 6 m were utilized. Scattering patterns were recorded for 20 minutes at each instrument configuration. The data were corrected for neutron transmission, dark current, empty beam scattering and detector efficiency, and normalized to absolute intensities using the empty beam intensity normalization technique. The corrected 2D data showed no scattering intensity asymmetries and were thus radially averaged to give scattering intensity I(Q) vs. momentum transfer (Q) curves. All corrections and normalizations were performed using the ORNL KCL routines. Modeling of the SANS data was pursued using the polydisperse hard sphere (PDHS) model implemented in the PRINSAS software package in order to calculate surface area/roughness of the porous films formed in 5 wt.% NaCl solutions [45-47].

Surface porosity of a duplicate set of 25 mm x 25 mm x 1.5 mm AZ31B and E717 test samples immersed for 24 h in H_2O + 5 wt.% NaCl was also characterized by gas adsorption of N_2 at 77 K using a Quantachrome Autosorb 1 C instrument with ASiQwin 2.0 data processing software for comparison with the SANS PDHS model results. Strips ~7.5 mm wide x 25 mm long were cut from the corroded AZ31B and E717 test samples using a low speed diamond saw in order to fit

into the instrument's sample holder. The strip samples were outgassed under vacuum at 200°C for ~2-3 hours to remove any adsorbed moisture prior to the N_2 adsorption. The results were fitted with the Brunauer-Emmett–Teller (BET) equation to calculate the surface area [48].

Microstructural characterization of the test samples was pursued by x-ray diffraction (XRD), scanning electron microscopy (SEM) with energy dispersive x-ray analysis (EDS), and STEM. The specimens for TEM analysis were prepared via the focus ion beam (FIB) milling technique by the in-situ lift-out method using a Hitachi NB5000 FIB-SEM. A carbon and tungsten overlayer was deposited to protect the exposed top surface of the film during ion milling (evaporating carbon first preserves the surface before using ion beam induced deposition of W). Further details of the sample preparation and analysis methodology are provided in reference 32.

Table 1. Alloy chemical composition of AZ31B and E717 sheet and plate samples determined by inductively coupled plasma atomic emission spectroscopy (ICP-AES). Plate sample alloys of AZ31B and E717 were from the same materials batches as used in references 32, 33. The E717 contains < 0.5 wt.% Nd, the exact level of Nd is considered proprietary.

Alloy	Composition weight % (wt.%)								
	Mg	Al	Zn	Zr	Mn	Nd	*Fe	Cu	Ni
AZ31B sheet	95.47	3.05	1.00	<0.001	0.46	<0.001	0.001, 0.002	0.001	0.001
E717 sheet	Bal.	0.004	1.49	0.31	0.008	< 0.5	0.0007, 0.007, 0.008	0.001	0.001
AZ31B plate	95.64	3.03	1.06	0.001	0.25	<0.001	0.006, 0.007	0.001	0.001
E717 plate	Bal.	<0.001	1.18	0.25	0.007	<0.5	0.004, 0.004	<0.001	0.001

*Some scatter in the range of Fe impurity level was found in the E717 sheet material. Data for Fe levels from 2 different measurements for AZ31B sheet, AZ31B plate, and E717 plate; and 3 different measurements for E717 sheet are shown in the table. Note that the test samples were polished to remove all residual surface finish prior to compositional analysis, as steel processing rolls can impart Fe impurities to the sheet surface during manufacture. Such surface contamination does not appear to be the source of the variation in Fe level detected for E717 sheet.

Results

SANS Data

Figures 1 a,b show SANS scattering intensity I(Q) vs. momentum transfer (Q) curves obtained for AZ31B and E717 as-received (1200 grit surface finish) and after 24 h immersion in H_2O, D_2O, H_2O + 5 wt.% NaCl, and D_2O + 5 wt.% NaCl. At small Q values, forward scattering occurs, which contains information about the scattering contrast and number density or volume fraction of scatterers. At high Q values, surface scattering is found, giving information about the surface area and its roughness. Porod representation plots of the SANS data are shown in Figs. 1 c,d for AZ31B and E717, respectively. The Porod representation, $I(Q)*Q^4$ vs. Q, normalizes regions of scattering from smooth surfaces to a zero slope. Peaks that may appear in the Porod representation originate from a predominance of scattering objects in a preferential, narrow size range [39, 40, 43].

The SANS dataset for both AZ31B and E717 assessed potential features in the range of ~2 nm (large Q values) to ~100 nm (small Q values). Features larger than ~100 nm were not resolved due to strong and multiple scattering from these AZ31B and E717 samples. No significant scattering changes were observed in as-received (unreacted) AZ31B and E717 metal vs. 24 h exposure in H_2O or D_2O (the respective scattering curves overlap each other in the Fig. 1 plots). This indicates that the 24 h exposure to water (water-formed films) did not result in sufficient nanoscale porosity or other feature changes in the ~2-100 nm range for SANS to detect. However, significant scattering changes were observed on exposure in H_2O or D_2O containing 5 wt.% NaCl. Further, scattering intensity from the D_2O + 5 wt.% NaCl exposed AZ31B and E717 was ~½ to 1 order of magnitude greater than from H_2O + 5 wt.% NaCl.

The slopes of the SANS curves contain statistical information about the dominant structural features at the respective length scales. No extended regions of constant slope were found in the scattering curves for either alloy (Fig. 1). The SANS data curves exhibited continuous, gradual slope changes. At small values of momentum transfer Q, i.e. roughly $Q < 0.01$ Å^{-1}, negative slopes of the scattering curves between 2 and 3 were observed, and indicate dominance of particle scattering. All samples showed a gradual transition to negative slopes from 3 to 4 beginning at roughly $Q > \approx 0.01$ Å^{-1}, which is indicative of scattering from rough interfaces.

These findings indicate that no preferred feature sizes resulted from exposure of AZ31B and E717 to the salt solutions, with a wide distribution of features in the ~30-100 nm size range evident in the particle scattering up to $Q \approx 0.01$ Å^{-1}, and rough internal surfaces at $Q > \approx 0.01$ Å^{-1}.

SEM Surface and Cross-Section Characterization

Figure 2 shows SEM surface images for the AZ31B and E717 SANS samples after 24 h in D_2O and D_2O + 5 wt.% NaCl. Similar results were also observed for H_2O exposures (not shown in Fig 2). In D_2O, little surface corrosion was evident, with the as-prepared 1200 grit surface finish still visible on the sample surfaces (vertical scratch lines in Figs. 2 a, c). In contrast, exposure to D_2O + 5 wt.% NaCl resulted in extensive corrosion and surface film formation. Loose corrosion products were observed on the test samples and remaining in the beaker after removal from the 5 wt.% NaCl solutions. The corrosion products formed in 5 wt.% NaCl solution for both AZ31B and E717 were highly heterogeneous and non-uniform, with local evidence of surface cracking, film spallation, and loosely adherent surface corrosion products. Higher magnification SEM surface images are shown in Fig. 3, which indicate a wide range of surface morphologies was formed, including cellular, needle-like, filamentous, and rough appearing structures. Analysis by XRD indicated that the primary corrosion product formed in the 5 wt.% NaCl solutions was $Mg(OH)_2$ (only peaks for $Mg(OH)_2$ and Mg metal were observed). Note that $Mg(OD)_2$ was likely formed in D_2O + 5 wt.% NaCl solutions, for simplicity Mg hydroxide formed in both H_2O and D_2O salt solutions will be referred to as $Mg(OH)_2$ in the presentation and discussion of the film microstructure.

The films formed by AZ31B and E717 after 24 h in D_2O and H_2O were considered too thin for SEM cross-section analysis. Scanning electron microscopy sample cross-sections of 5 wt.% NaCl exposed AZ31B and E717 are shown in Fig 4. The extent of attack was nonuniform, with film regions varying locally from only a few microns to over ~100 microns thick (Figs 4 a,b). It should be noted that the surface film was loosely adherent, and it is likely that local loss of surface film in some sample regions occurred during handling and/or cross-section preparation.

Higher magnification SEM images of the film cross-sections suggested a highly irregular duplex film, with the outer film regions generally appearing porous and loosely adherent, and the inner film regions more dense in appearance but frequently with cracks (Fig 4 c,d). Based on XRD data, the outer film regions are $Mg(OH)_2$. The inner film regions were consistent in morphological appearance with MgO or MgO-$Mg(OH)_2$ mixtures (based on previous work on these alloys in reference 32). Analysis of the film cross-sections by SEM/EDS revealed the presence of minor amounts of Cl, and in some cases Na, in both the outer and inner film regions (Cl and Na peaks were generally higher at inner film regions than outer).

TEM Analysis of SANS test sample 24 h D_2O Formed Films

High angle annular dark field (HAADF) images of the film cross-sections formed on AZ31B and E717 after 24 h in D_2O are shown in Fig. 5. The film on AZ31B (Fig. 5a) was relatively uniform and on the order of 100 nm thick in the imaged region. Some pore areas (dark circular regions) were apparent in the film, although it is not clear if those are inherent to the structure or the result of local beam damage in the STEM imaging [32]. The film structure was similar to that reported for 24 H_2O exposed AZ31B in earlier work by the present authors and consistent with a partially hydrated, MgO-base film [32, 33]. (Secondary ion mass spectroscopy analysis in the previous work [32, 33] indicated that the 24 h water-formed films on AZ31B and E717 contained H throughout, with higher levels of H at the film-liquid surface, decreasing into the film toward the metal-film interface. The form of this partial hydration was not determined, and could be either from locally intermixed $Mg(OH)_2$ in the MgO or some other type of H species incorporation). Bright nanoscale metal particles were also observed in the AZ31B, both in the underlying alloy and incorporated in the surface MgO-base film (indicative of an inward film growth mechanism). EDS analysis indicated that these particles were Al-Mn rich, consistent with recent TEM study of AZ31B H24 alloy and films [38].

The film region imaged on E717 after 24 h in D_2O (Fig. 5b) was duplex, with an inner, somewhat uniform region ~50 nm thick, consistent with partially-hydrated MgO, and an outer region of a filamentous morphology extending up to an additional several hundred nm outward in some locations, consistent with $Mg(OH)_2$ based on previous STEM study of 24 h H_2O

exposed E717 [32]. Bright nanoscale metal particles were again evident in the underlying alloy. Previous work identified this phase as Zn_2Zr_3 [32]. It should be noted that outer surface $Mg(OH)_2$ was not consistently observed in our previous study of film formation by AZ31B and E717 in H_2O when imaged in cross-section STEM [32]. This is considered a consequence of the local nature of TEM imaging, and the generally heterogeneous and varied nature of film formation across the surface of Mg alloys. The tendency of $Mg(OH)_2$ to form as a loosely adherent surface structure also makes it challenging to fully retain it during sample handling and preparation. In x-ray photoelectron spectroscopy analysis (~400 micron spot size) of the films formed on AZ31B and E717 in water, $Mg(OH)_2$ (along with MgO and $MgCO_3$) was always detected at the film outer surface [32]. Therefore, the absence of surface $Mg(OH)_2$ observable in the 24 h D_2O AZ31B cross-section STEM image of the present work (Fig 5a) vs. E717 (Fig. 5b) is likely simply a local effect of the particular region imaged, and not necessarily evidence of a difference in $Mg(OH)_2$ formation tendency in water for these two alloys.

TEM Analysis of SANS test sample 24 h D_2O+ 5 wt.% NaCl Formed Films

The film formed on AZ31B after 24 h in D_2O + 5 wt.% NaCl was orders of magnitude thicker than that formed in D_2O (e.g. Figs. 2,4, and 6a vs. Fig. 5a). The region imaged (Fig. 6) consisted of a several micron thick, dense inner layer consistent with MgO at the metal-film interface, which transitioned to a filamentous, porous and thick outer $Mg(OH)_2$ (identification based on morphology and bulk XRD analysis). It should be noted that the films formed in both D_2O and H_2O with 5 wt.% NaCl were quite heterogeneous, with others regions imaged for AZ31B indicating an inner MgO-base layer only on the order of 50-100 nm, although again transitioning to a thick, outer, filamentous and porous $Mg(OH)_2$. The size and morphology of the filamentous $Mg(OH)_2$ varied from quite fine near the inner MgO-base layer interface, with irregular shaped pores as small as ~20-40 nm dimensions in some locations, to outer fibers at the $Mg(OH)_2$-liquid interface on the order of micron diameters (Figs. 6 b-d).

Figure 7 shows a dark field (DF) STEM image of the film cross-section and corresponding EDS maps for a region of the film formed on AZ31B from Fig. 6a. Aluminum was detected throughout the inner MgO-base layer, with a degree of Zn enrichment at the metal-film interface.

Similar segregation was observed in AZ31B H_2O formed MgO-base films from previous work [32], although the degree of Zn enrichment appeared qualitatively less continuous in the NaCl solution exposed AZ31B. The porous $Mg(OH)_2$ adjacent to the inner MgO-base layer appeared to be composed solely of Mg and O (H cannot be mapped by EDS), with no Al or other AZ31B alloy elements detected.

DF STEM images of the film cross-section formed on E717 after 24 h in H_2O and D_2O + 5 wt.% NaCl are shown in Fig. 8. Similar to the AZ31B, the structure was consistent with an inner MgO-base film and a thick, outer, porous $Mg(OH)_2$ with irregular pore sizes well below 100 nm dimensions in some areas. Figure 8c shows a region of the metal-film interface with a lesser extent of outer $Mg(OH)_2$ formation (or retention) in the FiB section imaged. The inner MgO-base layer was ~50-100 nm thick and somewhat irregular at the film-metal interface. Overlying the inner MgO was a laminar appearing, several hundred nm thick region consistent in imaging with $Mg(OH)_2$, from which filamentous $Mg(OH)_2$ appeared to branch irregularly outward. Elemental EDS maps of this region are shown in Fig. 9. A Zn-Nd rich particle was observed in the underlying metal, with a modest degree of Zn segregation to the metal-film interface and no evidence of Zr incorporation in the film. (H_2O-formed films on E717 in previous work showed a qualitatively stronger, better delineated Zn segregation at the metal-film interface, as well as Zn_2Zr_3 nanoparticle incorporation into MgO-base film [32]). For both 24 h NaCl solution exposed AZ31B and E717 of the present work, occasional Cl, and in one case, Na were detected in the film regions by STEM mapping.

In order to gain additional insight into the effects of NaCl on the earlier stages of film formation, an additional exposure set was conducted for 4 h in H_2O + 1 wt.% NaCl, with the shorter exposure time and lesser concentration of NaCl selected in an attempt to capture the film structure prior to the onset of extensive porous outer $Mg(OH)_2$ formation. Film cross-sections acquired by TEM and elemental maps are shown in Figs. 10 and 11. In the case of AZ31B (Fig. 10), the region imaged had already transitioned to porous $Mg(OH)_2$ formation. The structure was consistent with an inner, relatively planar and dense MgO-base layer on the order of 50 nm thick, which transitioned to outer branched, filamentous $Mg(OH)_2$ formation. The EDS maps indicated both Al in the inner MgO-base layer, but not the outer $Mg(OH)_2$, and segregation of Zn

to the metal-film interface. Chlorine was detected extending into the inner MgO-base film regions, to the vicinity of the film-metal interface.

Similar Cl penetration to the inner MgO-base film and the film-metal interface was also observed for the E717 (Fig. 11). The STEM image region for the E717 was consistent with a primarily MgO-base film, in the early stages of transition to an outer, laminar $Mg(OH)_2$. Features suggestive of pores in the inner MgO-base layer were also observed, but it was again not possible to definitively determine if these were inherent to the film structure or the result of beam damage. (Previous work noted that E717 H_2O formed films were particularly susceptible to beam damage [32]). The presence of Zn enrichment was detected at the film-metal interface region in the 4 h, 1wt.% NaCl exposed E717. Additionally, particles consistent with Zn_2Zr_3 were detected in the underlying alloy, and in some local areas were also present in the MgO-base film, again consistent with an inward film growth mechanism [32, 33].

Discussion

The SANS data showed no significant scattering changes for test samples of as-received metal AZ31B and E717 vs. after 24 h exposure in D_2O or H_2O. This finding is consistent with the relatively smooth surfaces evident by SEM surface analysis and the thin, relatively dense and protective MgO-base films evident in film cross-sections acquired by STEM (Figs. 2 a,c and 5). In contrast, significant changes in SANS scattering from both alloys resulted from exposure in 5 wt.% NaCl solution (Fig. 1). Based on the SEM and TEM analysis (Figs 2. b, d, 3, 6, and 8), the SANS data changes are attributed primarily to the thick, outer porous $Mg(OH)_2$ structures formed in the 5 wt.% NaCl solution by both alloys.

The intensities of the SANS scattering changes were ~0.5 to 1 order of magnitude higher in D_2O + 5 wt.% NaCl than H_2O + 5 wt.% NaCl for both alloys (Fig. 1). The neutron coherent scattering length density (SLD) for hydrogenated $Mg(OH)_2$ is $\sigma = 2.3*10^{-6}$ Å^{-2} and the SLD for deuterated $Mg(OD)_2$ is $\sigma = 7.33*10^{-6}$ Å^{-2}, assuming the same molar volumes for $Mg(OH)_2$ and $Mg(OD)_2$. With a zero SLD for the pore volumes, the contrasts between $Mg(OH)_2$ and $Mg(OD)_2$ matrix and embedded nanopores are proportional to the Mg hydroxides SLD squared. For protonated and deuterated Mg hydroxide, the difference in pore scattering contrast is close to 1

order of magnitude, and consistent with the enhanced scattering intensity observed for the sample reacted in D_2O + 5 wt.% NaCl as compared to the sample reacted in H_2O + 5 wt.%. This finding strongly suggests that the reaction layers formed in NaCl solutions responsible for the scattering changes detected in SANS consisted predominantly of Mg hydroxide.

The SEM and TEM analysis revealed the formation of porous $Mg(OH)_2$ with irregular thickness and structures over a wide range of length scales. To gain more insight into the hydroxide film nanoscale structure, modeling of the SANS data from the AZ31B and E717 exposed in H_2O + 5 wt.% NaCl and D_2O + 5 wt.% NaCl was pursued using the polydisperse hard sphere (PDHS) model implemented in the PRINSAS software package [45-47]. This model provides a quantitative representation of nanoscale porosity, and was developed to describe pore systems in coal, weathered rocks, and soils [46, 47, 49, 50]. It is based on fitting scattering data by a hard sphere model as a fractal assemblage of spheres to assess pore size distribution and surface roughness/surface area inside pores.

For this analysis, the SANS scattering data from the as-received (unreacted) metal samples were subtracted from the 5 wt.% NaCl solution metal sample scattering data, yielding scattering curves representing only the corrosion films formed on the front and back surfaces of the test samples. The analysis assumed all scattering was derived from the porous $Mg(OH)_2$, although it is certainly possible that some scattering also resulted from the roughened film-metal interface resulting from corrosion in NaCl solution. For intensity normalization, the combined average thickness of $Mg(OH)_2$ for both AZ31B and E717 was estimated to be 100 microns total (i.e, 50 microns each face), which was based on sample surface and cross-section images and the extent of corrosion observed.

Nanoscale porosities of ~ 40% in the $Mg(OH)_2$ formed in NaCl solutions for both AZ31B and E717 were indicated from the fitting of the data. Specific surface area distribution vs. fitted feature radius size plots from the PDHS modeling of the Mg hydroxide film SANS data is shown in Fig. 12. Specific surface areas (effectively internal roughness of the porous structure) on the order of ~100 m^2/cm^3 were calculated for AZ31B and E717 in both D_2O + 5 wt.% NaCl and H_2O

+ 5 wt.% NaCl. The modeled data indicate that more than 90% of the roughness surface area was located in structures fit with hard sphere radii smaller than 300 Å (Fig. 12).

Note that the PDHS approach models the porosity network and internal surface area/roughness as a function of a fractal assemblage of sphere feature radius size, i.e. the smaller the fitted sphere feature size, the more surface area/roughness that is registered. It does not explicitly assume that the pores in the $Mg(OH)_2$ of the present work were spherical, or that the actual $Mg(OH)_2$ pore sizes extended to Å size range. As evident in the STEM images (Figs 6, 8), the pores varied in both size and shape, with the smallest pore sizes in the ~20-40 nm range, effectively formed by the voids between filamentous $Mg(OH)_2$ morphologies. This pore size range was consistent with the negative slopes of the scattering curves between 2 and 3 at Q values < 0.01 Å^{-1} (which covered the size range of ~30-100 nm) where particle (pores in this case) dominated scattering was observed (Fig. 1).

The high surface areas estimated by the PDHS model are therefore best interpreted in the present work as an assessment of internal roughness within the porous $Mg(OH)_2$. Negative slopes between 3 and 4, indicative of scattering from rough interfaces (internal and external), were found beginning around $Q > 0.01$ Å^{-1} (the transition was gradual, not sharp) in the SANS scattering curves (Fig. 1). Assuming that all scattering resulted from porous $Mg(OH)_2$, using a density of 2.34 g/cm^3 for $Mg(OH)_2$, a specific surface area of 100 m^2/cm^3 from the SANS PDHS model translates to ~43 m^2/g. This is a surprisingly high surface area for a film formed by a corrosion process, and approaches the range exhibited by catalysts.

As an independent check on this high surface area derived by PDHS, a duplicate set of H_2O + 5 wt.% NaCl AZ31B and E717 test samples was evaluated for surface area by the BET method [48] using gas adsorption of N_2 at 77 K (i.e. the original SANS measured samples were not re-measured by BET). The surface area of the 1200 grit polished as-received metal test samples (no corrosion exposure) was too low to measure by BET. The nominal surface area per gram for the unreacted Mg alloys was ~9 x 10^{-4} m^2/g (based on test sample length, width, thickness dimensions and assuming a smooth surface with little added surface area). The BET measurement for an E717 test sample exposed for 24 h in 5 wt.% NaCl solution yielded a value

of ~2 m^2/g surface area, and ~0.2 m^2/g for a NaCl-exposed AZ31B test sample. These values are ~200-2000x higher than the nominal, unexposed metal surface area/g. (Note that XRD and surface SEM analysis of pre- and post- BET measurement samples did not indicate any significant film changes as a result of the 200°C vacuum exposure needed for outgassing prior to BET measurement).

The BET surface area per gram values were for the entire 1.5 mm thick test sample, metal and corrosion film. Assuming the BET surface porosity is due solely to the corrosion film, ~50 microns $Mg(OH)_2$ per face, ~100 microns total, the estimated mass of $Mg(OH)_2$ at 40% porosity is on the order of ~5% of the total mass of the test sample. Therefore, 2 m^2/g measured by BET for a 1.5 mm thick Mg alloy test sample with 100 microns total porous $Mg(OH)_2$ yields an estimated 40 m^2/g surface area for the porous $Mg(OH)_2$, which correlates well with the SANS PDHS assessed E717 sample. By similar estimation, the 0.2 m^2/g measured for the duplicate AZ31B 5 wt.% NaCl solution test sample yields an estimate of 4 m^2/g for the porous $Mg(OH)_2$, which is an order of magnitude lower than the AZ31B sample evaluated by SANS PDHS, although it is still a significant surface area increase over unreacted metal surface as previously noted.

The reason for the lower BET surface area for the duplicate 24 h NaCl solution exposed AZ31B vs. the SANS AZ31B sample is not known. It is hypothesized that the lower BET surface area value in this case may be a consequence of sample to sample corrosion variation over the short, 24 h exposure period and the nonuniform nature of Mg alloy corrosion in water + NaCl, with a lesser extent of porous $Mg(OH)_2$ on the AZ31B BET test sample than on the AZ31B SANS test sample. (The additional handling required to cut the corroded test samples to strips for BET analysis may also have resulted in some loss of the loosely adherent Mg hydroxide from the sample). It should be noted that SANS measurement captures total internal surface area, including internal features and disconnected porosity, whereas BET measurement is limited to assessment of only open, surface connected porosity. The formation of extensive disconnected porosity may also contribute to the lower surface area for the duplicate AZ31B measured by BET vs. SANS AZ31B, although if that were the case a similar, low BET surface area would

have been expected for the E717 duplicate as well, because the AZ31B and E717 corrosion film features from NaCl exposure were similar.

Exposure of both AZ31B and E717 for 24 h in 5 wt.% NaCl solutions resulted in rapid corrosion, with extensive, filamentous, and porous $Mg(OH)_2$ formation overlying far thinner MgO-base films Figs 6, 8). This is in contrast to the films formed by exposure of AZ31B and E717 for 24 h in pure water, which consisted primarily of thin, partially hydrated MgO (Figs 2, 5), with the outer film surface regions also containing minor amounts of $Mg(OH)_2$ and $Mg(CO)_3$ [32]. The highly porous nature of the $Mg(OH)_2$ outer film formed in NaCl solution would be expected to provide little to no protection from corrosion, and permit access of the liquid to the inner regions of the film and/or the film-metal interface. Further, for such thick $Mg(OH)_2$ films -tens of microns thick- to be formed (Fig 4), the inner MgO-base layer formed in NaCl solution cannot have been protective. The presence of Cl- is well established to both enhance Mg dissolution and disrupt the protectiveness of aqueous-formed $MgO/Mg(OH)_2$ films. These effects have been linked to enhanced dissolution and increased aqueous solubility by formation of $MgCl_2$ and/or Mg hydroxychloride complexes [9, 12, 13, 15, 21, 51], as well as possible cracking and rupture of the inner film regions [e.g. 17, 22]. In the present work, Cl was detected in the inner MgO-base layer, and extending to the metal-film interface (Figs. 10, 11).

The inner MgO-base film regions formed in NaCl solutions appeared relatively dense in the STEM sections analyzed (Figs 6, 8, 10, 11). Some porosity was also observed in the inner MgO-base film regions; however, it was not possible to definitively distinguish if this porosity resulted from beam damage in the STEM or was inherent to the film structure. The relatively dense inner MgO-base film regions and the morphology of the transition from the inner MgO-base film region to the outer porous $Mg(OH)_2$ suggest that at least some of the breakdown occurred at the $MgO-Mg(OH)_2$ interface. It is speculated that corrosion may proceed at least in part by a manner analogous to the high-temperature paralinear oxidation of SiC in the presence of water vapor, where initially formed SiO_2 is degraded at the SiO_2-gas interface by volatilization and loss of SiO_2 via Si-oxyhydroxide formation [e.g. 52, 53]. The reaction reaches a steady-state like condition, with an inward-moving, constantly-thinned SiO_2 film rapidly consuming material cross-section. In the case of high pressure steam, this results in an oxidized cross-section of an

inner, thin, dense, and amorphous SiO_2 layer and outer, thick porous crystalline SiO_2 [53]. Increasing rates of H_2 production during corrosion of Mg alloys in 3 wt.% NaCl solution, after an initial, slow incubation period, transitioning to steady-state, linear production of H_2 has been reported [54], which is consistent with this paralinear oxidation analogy speculation. It has also been reported [55] that in the initial stages of immersion, the corrosion may initially slow until a degradation of the surface film occurs and Mg dissolution starts to accelerate; the transition from initially protective to degraded state may take a few hours in a chloride containing solution.

The porous morphologies and high surface area of the $Mg(OH)_2$ formed by AZ31B and E717 in 5 wt.% NaCl solution Fig. 3) are strikingly similar to that reported for the synthesis of nanoscale $Mg(OH)_2$ by precipitation-based routes [56-59]. This suggest at least some of the $Mg(OH)_2$ formation from Mg corrosion in NaCl solutions results from Mg species dissolution and re-precipitation in the surface regions. Laminar morphologies present at the MgO-$Mg(OH)_2$ interface (Fig. 8c) also suggest a degree of direct conversion of MgO to $Mg(OH)_2$. Filamentous morphologies of $Mg(OH)_2$ nucleated (or ruptured) and grew outward from the $Mg(OH)_2$ layer, presumably aided by continued growth into supersaturated solution. It is speculated that these filamentous $Mg(OH)_2$ growths can then act as sites for further nucleation and/or precipitation deposition of $Mg(OH)_2$, with the continuously increasing surface area leading to the thick, filamentous and porous $Mg(OH)_2$ structures observed (Fig 6, 8). Even taking the lower BET surface area of 4 m^2/g for the NaCl solution exposed AZ31B, there is considerable surface area evolved in the porous $Mg(OH)_2$, consistent with a rapid, nonprotective corrosion. Recent study [60] has also shown that corrosion of Mg in saturated $Mg(OH)_2$, particularly at an anodic potential, has a surface film with inner and outer layer morphologies very similar to those in the chloride containing solutions observed in the present work. This hypothesized comparison suggests that growth of filamentous $Mg(OH)_2$ may result from increased anodic dissolution of Mg.

Further work is needed to clarify the exact mechanism(s) by which Cl acts to destabilize protective film growth: increased dissolution, increased film growth rates, stress rupture of film (phase volume changes and/or H_2 gas evolution), etc. The evaluation of SANS in the present work shows it has good potential to provide new insight into Mg corrosion, particularly the

evolution of porous $Mg(OH)_2$ when D_2O + NaCl is used. A key advantage of SANS is the ability to obtain data over the entire sample, which is beneficial given the non-uniform and heterogeneous nature of Mg corrosion, and can complement more local techniques such as TEM imaging. A further advantage is the potential to obtain data in-situ during Mg corrosion as a function of exposure time, i.e. one could monitor surface area changes as a function of exposure time in-situ for Mg alloys in NaCl solutions.

SANS may also prove useful in characterizing possible roughness/surface area changes at the film-metal interface vs. exposure time. This could be accomplished, for example, by evaluating corroded Mg samples with the surface film regions removed by chromate dissolution prior to SANS study. SANS could also potentially provide new insight into anodic film formation relative to the current debate regarding the mechanism of the negative difference effect for Mg, whereby H_2 evolution is observed to increase with increasing anodic potential. Knowledge gained by ex-situ or in-situ SANS study of the evolution of surface area/roughness vs. potential and/or time may help clarify the proposed mechanisms, for which filamentous/dendritic corrosion products have been reported [20, 35, 61-66]

Summary and Conclusions

Small angle neutron scattering and TEM analysis were used to study film formation by AZ31B and E717 in water with NaCl.

1) SANS scattering was not sensitive to the relatively dense and protective MgO-base films formed by AZ31B and E717 in 24 h exposures in H_2O or D_2O. However, significant scattering changes were observed when the alloys were exposed to NaCl solutions, and were attributed to extensive, nanoporous $Mg(OH)_2$ formation. The use of D_2O + NaCl enhanced the scattering resulting from corrosion, presumably by the formation of $Mg(OD)_2$, due to the enhanced SLD of D. These findings indicate that SANS shows promise as a new technique for the study of Mg corrosion, particularly the transition to porous $Mg(OH)_2$ formation and rapid corrosion resulting from film breakdown. A key advantage of SANS is the ability to obtain data over the entire sample, which is of particular interest given the locally non-uniform nature of Mg corrosion,

making it a good complement to more local structural characterization techniques such as SEM/TEM.

2) The SANS PDHS model shows good early promise to quantify the surface area/roughness resulting from the porous $Mg(OH)_2$ structures formed from corrosion of Mg in water with NaCl, although further work is needed to confirm its utility and accuracy for Mg corrosion. TEM, SANS, and BET all indicated that exposure in 5 wt.% NaCl solution resulted in extensive, nanoporous $Mg(OH)_2$ formation with very high surface areas, estimated to be in the rage of 4 to 40 m^2/g. Such high surface area is consistent with the rapid, non-protective corrosion observed, and has implications for mechanistic understanding of how the films breakdown and the porous $Mg(OH)_2$ continuous to grow

3) Analysis by SEM and STEM indicated that the film structure consisted of an inner MgO-base layer, that transitioned to laminar and then highly filamentous and porous $Mg(OH)_2$. Chlorine penetrated the inner MgO-base layer to the vicinity of the film-metal interface. Further work will be required to determine the mechanism(s) responsible for how NaCl disrupted film stability. The film structures observed suggested a combination of preferential growth (or rupture) of filamentous $Mg(OH)_2$ from an intermediate laminar $Mg(OH)_2$ film between inner relatively dense MgO and outer porous $Mg(OH)_2$. Further filamentous $Mg(OH)_2$ growth supported by supersaturation and precipitation follows, yielding porous, high surface area $Mg(OH)_2$ that permits continued access of liquid to the inner film regions and/or film-metal interface. A speculated framework interpretation film growth mechanism based on classic, paralinear type high-temperature oxidation phenomena was forwarded.

Acknowledgements

The authors thank D.W. Coffey, T.M. Lowe, T. Geer and T.L. Jordan for assistance with the experimental work. G. Muralidharan, D.N. Leonard, and B.A. Pint provided helpful comments and suggestions on the results and manuscript. The authors also thank E. Cakmak and R.A. Meisner for analysis of xrd data. This research was sponsored by the U.S. Department of Energy,

Energy Efficiency & Renewable Energy Vehicle Technologies Office. A portion of this research conducted at ORNL's High Flux Isotope Reactor and the Center for Nanophase Materials Sciences, which is sponsored by the Scientific User Facilities Division, Office of Basic Energy Sciences, U.S. Department of Energy.

Appendix A: Analysis of Materials by Small Angle Neutron Scattering

Small angle neutron scattering (SANS) is a well-established technique that uses elastic neutron scattering to probe the structural characteristics of materials in the nanoscale length regime [39, 40, 67-70]. In metallurgy, it has classically been used to study nanoscale precipitates and pores [e.g. 39]. Small angle neutron scattering is qualitatively similar to small angle x-ray scattering (SAXS), both probe structures in the nanoscale size regime [40]. Unlike SAXS, the beam size for SANS can be quite large, beam cross-sections can be several cm^2, with deep penetration of neutrons on the order of millimeters [40]. Thus, the scattering curve results from SANS represents a large volume of sample material and the technique is suitable for analysis of bulk samples, whereas SAXS is typically limited to relatively thin sample cross-sections (< 100 microns) [40]. A key potential advantage of SANS for the study of aqueous corrosion of metals (such as Mg) is that the neutron scattering cross section for hydrogen is large, whereas with SAXS, x-ray scattering from hydrogen is low due to its low atomic number, and easily masked by other elements. Further, hydrogen and deuterium have significantly different neutron scattering properties, allowing assessment of scattering contrasts arising from such differing sources as hydroxides and pore structures formed on reaction of metals with H_2O vs. D_2O.

A simplified schematic of a SANS scattering experiment is shown in Fig. A1 [40, 71]. The neutron beam penetrates through the sample, with transmitted incident and scattered neutrons registered by a position sensitive 2 dimensional x-y detector [40]. SANS measures the scattered intensity $I(Q)$ of the neutrons as a function of the scattering vector Q. The scattering vector is defined by $Q = \frac{4\pi \sin\theta}{\lambda}$, with θ the angle of scatter and λ the neutron wavelength [39, 40, 72, 73]. The length scale probed is proportionate to λ/θ, generally in the range of 1 to a few hundred nm [39, 40].

Scattered intensity arises from spatial changes in the nuclear scattering length densities (SLD), ρ_i^*, between a nano-scale phase and the medium surrounding it [e.g. after background discussion in 72, 73]. The SLD of phase j is given by:

$$\rho_j^* = \sum_{i=1}^{n} b_i \frac{\rho_j N_A}{M_i} \quad (1),$$

where b_i is the bound coherent scattering length of atom i, N the total number of atoms in the molecule, ρ_j is the mass density, N_A is the Avogadro constant and M_i is the molar mass. Scattering contrast in corroded metallic samples arises primarily from the difference in the coherent scattering length densities (SLD) of the phases formed during corrosion and any resultant nanopore spaces (zero SLD) within it.

Small angle neutron scattering data can be analyzed in reciprocal space by least-square fitting to model functions or in real space after Fourier transformation [e.g. after background discussion in 72, 73]. Both techniques yield information about the shape and size or size ranges of scatterers. The invariant Z, defined by

$$Z = \int_0^\infty Q^2 I(Q) dQ \quad (2),$$

yields direct, model-independent information about the scattering contrast and volume of scatterers. For a two-phase system the invariant is given by:

$$Z = 2\pi^2 \phi_1 (1 - \phi_1)(\rho_1^* - \rho_2^*)^2 \quad (3),$$

with φ_1 equal to the volume fraction of phase 1 and ρ_1* its coherent SLD. After reducing the data [e.g. 74], the SANS scattering curves can then potentially yield precipitate size distributions, porosities, pore distribution geometry (mass fractal behavior), the nature of interfaces (surface fractal behavior), characteristic lengths associated with the fractal behavior, and the surface area to volume ratio.

References

1. A. A. Luo, Jom-Journal of the Minerals Metals & Materials Society, 54, 42 (2002).

2. C. Blawert, N. Hort and K. U. Kainer, *Transactions of the Indian Institute of Metals*, **57**, 397 (2004).

3. I. Johnson and H. N. Liu, *Plos One*, **8** (2013).

4. B. Sakintuna, F. Lamari-Darkrim and M. Hirscher, Int. J. Hydrogen Energy, 32, 1121 (2007).

5. M. Kappes, M. Iannuzzi and R. M. Carranza, *J. Electrochem. Soc.*, **160**, C168 (2013).

6. T. Khoo, P. C. Howlett, M. Tsagouria, D. R. MacFarlane and M. Forsyth, *Electrochim. Acta*, **58**, 583 (2011).

7. J. O. G. Posada and P. J. Hall, *Int. J. Hydrogen Energy*, **39**, 8321 (2014).

8. G. L. Makar and J. Kruger, *Int. Mater. Rev.*, **38**, 138 (1993).

9. G. L. Song and A. Atrens, *Adv. Eng. Mater.*, **1**, 11 (1999).

10. J. E. Gray and B. Luan, *J. Alloys Compd.*, **336**, 88 (2002).

11. R. C. Zeng, J. Zhang, W. J. Huang, W. Dietzel, K. U. Kainer, C. Blawert and W. Ke, *Transactions of Nonferrous Metals Society of China*, **16**, S763 (2006).

12. G. Williams and H. N. McMurray, *J. Electrochem. Soc.*, **155**, C340 (2008).

13. F. Y. Cao, Z. M. Shi, J. Hofstetter, P. J. Uggowitzer, G. L. Song, M. Liu and A. Atrens, *Corros. Sci.*, **75**, 78 (2013).

14. E. Ghali, W. Dietzel and K. U. Kainer, *J. Mater. Eng. Perform.*, **13**, 7 (2004).

15. I. Giner, O. Ozcan, G. Grundmeier, *Corros. Sci.*, **87**, 51 (2014).

16. N. Hara, Y. Kobayashi, D. Kagaya and N. Akao, *Corros. Sci.*, **49**, 166 (2007).

17. J. R. Kish, Y. Hu, J. Li, W. Zheng and J. R. McDermid, *Corrosion*, **68**, 468 (2012).

18. O. Lunder, J. E. Lein, S. M. Hesjevik, T. K. Aune and K. Nisancioglu, *Werkstoffe Und Korrosion-Materials and Corrosion*, **45**, 331 (1994).

19. A. Pardo, M. C. Merino, A. E. Coy, R. Arrabal, F. Viejo and E. Matykina, *Corros. Sci.*, **50**, 823 (2008).

20. G. Song, A. Atrens, D. St John, X. Wu and J. Nairn, *Corros. Sci.*, **39**, 1981 (1997).

21. L. Wang, B. P. Zhang and T. Shinohara, *Materials & Design*, **31**, 857 (2010).

22. H. B. Yao, Y. Li and A. T. S. Wee, *Appl. Surf. Sci.*, **158**, 112 (2000).

23. S. J. Xia, R. Yue, R. G. Rateick and V. I. Birss, *J. Electrochem. Soc.*, **151**, B179 (2004).

24. P. Schmutz, V. Guillaumin, R. S. Lillard, J. A. Lillard and G. S. Frankel, *J. Electrochem. Soc.*, **150**, B99 (2003).

25. A.D. King, N. Birbilis and J. R. Scully, *Electrochim. Acta*, **121**, 394 (2014).

26. M. Taheri, M. Danaie and J. R. Kish, *J. Electrochem. Soc.*, **161**, C89 (2014).

27. V. Fournier, P. Marcus and I. Olefjord, *Surf. Interface Anal.*, **34**, 494 (2002).

28. M. Jonsson, D. Persson and D. Thierry, *Corros. Sci.*, **49**, 1540 (2007).

29. M. Taheri, R. C. Phillips, J. R. Kish and G. A. Botton, *Corros. Sci.*, **59**, 222 (2012).

30. J. H. Nordlien, S. Ono, N. Masuko and K. Nisancioglu, *Corros. Sci.*, **39**, 1397 (1997).

31. R. C. Phillips and J. R. Kish, *Corrosion*, **69**, 813 (2013).

32. K. A. Unocic, H. H. Elsentriecy, M. P. Brady, H. M. Meyer, G. L. Song, M. Fayek, R. A. Meisner and B. Davis, *J. Electrochem. Soc.*, **161**, C302 (2014).

33. M. P. Brady, M. Fayek, H. H. Elsentriecy, K. A. Unocic, L. M. Anovitz, J. R. Keiser, G. L. Song and B. Davis, *J. Electrochem. Soc.*, **161**, C395 (2014).

34. M. Danaie, R. M. Asmussen, P. Jakupi, D. W. Shoesmith and G. A. Botton, *Corros. Sci.*, **77**, 151 (2013).

35. M. Taheri, J. R. Kish, N. Birbilis, M. Danaie, E. A. McNally and J. R. McDermid, *Electrochim. Acta*, **116**, 396 (2014).

36. G. Baril and N. Pebere, *Corros. Sci.*, **43**, 471 (2001).

37. D.A. Vermilyea and C. F. Kirk, *J. Electrochem. Soc.*, **116**, 1487 (1969).

38. Z.P. Cano, M. Danaie, J.R. Kish, J.R. McDermid, G.A. Botton, and G. Williams (2014) Corrosion In-Press. doi: http://dx.doi.org/10.5006/1384

39. P. Fratzl, *J. Appl. Crystallogr.*, **36**, 397 (2003).

40. A. J. Allen, *J. Am. Ceram. Soc.*, **88**, 1367 (2005).

41. M. Schober, C. Lerchbacher, E. Eidenberger, P. Staron, H. Clemens and H. Leitner, *Intermetallics*, **18**, 1553 (2010).

42. D. V. Pugh, A. Dursun and S. G. Corcoran, *J. Mater. Res.*, **18**, 216 (2003).

43. G. Rother, J. R. Keiser, M. P. Brady, K. A. Unocic, L. M. Anovitz, K. C. Littrell, R. A. Peascoe-Meisner, M. L. Santella, D. J. Wesolowski and D. R. Cole, *Corros. Sci.*, **58**, 121 (2012).

44. X.P. Niu, T. Skszek, M. Fabischek, A. Zak, *Mater. Sci. For.*, **783-786**, 431(2014).

45. A. L. Hinde, *J. Appl. Crystallogr.*, **37**, 1020 (2004).

46. A. P. Radlinski, M. A. Ioannidis, A. L. Hinde, M. Hainbuchner, M. Baron, H. Rauch and S. R. Kline, *J. Colloid Interface Sci.*, **274**, 607 (2004).

47. A. P. Radlinski, M. Mastalerz, A. L. Hinde, A. Hainbuchner, H. Rauch, M. Baron, J. S. Lin, L. Fan and P. Thiyagarajan, *International Journal of Coal Geology*, **59**, 245 (2004).

48. S. Brunauer, P.H. Emmett, E. Teller, *J Am Chem Soc*, 60 (1938).

49. A. K. Navarre-Sitchler, D. R. Cole, G. Rother, L. X. Jin, H. L. Buss and S. L. Brantley, *Geochim. Cosmochim. Acta*, **109**, 400 (2013).

50. L. X. Jin, R. Mathur, G. Rother, D. Cole, E. Bazilevskaya, J. Williams, A. Carone and S. Brantley, *Chem. Geol.*, **356**, 50 (2013).

51. M. Altmaier, V. Metz, V. Neck, R. Muller and T. Fanghanel, *Geochim. Cosmochim. Acta*, **67**, 3595 (2003).

52. E. J. Opila and R. E. Hann, *J. Am. Ceram. Soc.*, **80**, 197 (1997).

53. K. L. More, P. F. Tortorelli, M. K. Ferber and J. R. Keiser, *J. Am. Ceram. Soc.*, **83**, 211 (2000).

54. M. C. Zhao, P. Schmutz, S. Brunner, M. Liu, G. L. Song and A. Atrens, *Corros. Sci.*, **51**, 1277 (2009).

55. Z. Li, G.-L. Song, S. Song, , *Electrochimica Acta*, **115**, 56(2014)

56. Y. Ding, G. T. Zhang, H. Wu, B. Hai, L. B. Wang and Y. T. Qian, *Chem. Mater.*, **13**, 435 (2001).

57. C. Henrist, J. P. Mathieu, C. Vogels, A. Rulmont and R. Cloots, *J. Cryst. Growth*, **249**, 321 (2003).

58. P.S. Das, A.Dey, A. K. Mandala, N. Dey, A.K. Mukhopadhyay, *J. Advanced Ceramics*, **2** (2), 173 (2013). DOI: 10.1007/s40145-013-0058-9

59. C. L. Yan, D. F. Xue, L. J. Zou, X. X. Yan and W. Wang, *J. Cryst. Growth*, **282**, 448 (2005).

60. G.-L. Song and K.A. Unocic, submitted.

61. G. S. Frankel, A. Samaniego and N. Birbilis, *Corros. Sci.*, **70**, 104 (2013).

62. N. Birbilis, A. D. King, S. Thomas, G. S. Frankel and J. R. Scully, *Electrochim. Acta*, **132**, 277 (2014).

63. G. Williams, H. A. Dafydd and R. Grace, *Electrochim. Acta*, **109**, 489 (2013).

64. L. Rossrucker, K. J. J. Mayrhofer, G. S. Frankel and N. Birbilis, *J. Electrochem. Soc.*, **161**, C115 (2014).

65. Z Shi, F Cao, GL Song, A. Atrens, *Corros. Sci.*, **88**, 434 (2014).

66. S. Thomas, N.V. Medhekar, G.S. Frankel, N. Birbilis, Current Opinion in Solid State and Materials Science, in press DOI: 10.1016/j.cossms.2014.09.005

67. B. Hammouda, Probing Nanoscale Structures: The SANS Toolbox (2009). http://www.ncnr .nist.gov/staff/hammouda/the_sans_toolbox.pdf

68. L.A. Feigin and D.I. Svergun, Structure analysis by small-angle X-ray and neutron scattering,. Plenum Press. New York.. (1987) http://www.embl-hamburg.de/biosaxs/reprints/feigin_svergun_1987.pdf

69. A. Guinier and G. Fournet, Small Angle Scattering of X-rays. New York: John Wiley (1955)..

70. O. Glatter O. and O. Kratky, Small Angle X-ray Scattering. Academic Press, London, UK (1982).

71. NIST Center for Neutron Research, National Institute of Standards and Technology 100 Bureau Drive, MS 6100, Gaithersburg, MD 20899-6100. http://www.ncnr.nist.gov/programs/sans/

72. L.M. Anovitz, H-W Wang, D.R. Cole, J. Sheets, G. Rother, D.D. Faulder, and M. Walters, Analysis of Multiscale Porosity at the Coso Geothermal Field. PROCEEDINGS, Thirty-Eighth Workshop on Geothermal Reservoir Engineering Stanford University, Stanford, California, February 11-13, 2013 SGP-TR-198

73. L.M. Anovitz, G. Rother, and D.R. Cole, Characterization of rock pore features in geothermal systems using small angle neutron scattering (SANS). PROCEEDINGS, Thirty-Sixth Workshop on Geothermal Reservoir Engineering Stanford University, Stanford, California, January 31 - February 2, 2011 SGP-TR-191

74. S.R. Kline, J. Appl. Cryst., **39,** 895 (2006).

Figure Captions

Figure 1-SANS scattering curves (a,b) and Porod representation (c,d) for AZ31B and E717. The black as-received, red 24 h D_2O, and green 24 h H_2O data points overlap considerably, such that they are not individually distinguishable in above plots.

Figure 2- Surface SEM images of AZ31B and E717 after 24 h in D_2O (a,c) or 24 h in D_2O with 5 wt.% NaCl (b,d). Images (a,c) backscatter mode and images (b,d) secondary mode

Figure 3- Surface secondary mode SEM images of AZ31B (a,c,e) and E717 (b,d,f) after 24 h in D_2O with 5 wt.% NaCl showing wide morphological variation of $Mg(OH)_2$ –base surface products formed.

Figure 4- Cross-section backscatter mode SEM images of AZ31B and E717 after 24 h in D_2O or H_2O with 5 wt.% NaCl showing low magnification views illustrating non-uniform attack (a,b) and typical higher magnification images of retained scale regions (some outer film spallation during sample handling and preparation occurred).

Figure 5- HAADF STEM images of film cross-sections formed on AZ31B (a) and E717 (b) after 24 h in D_2O.

Figure 6- AZ31B after 24 h in D_2O with 5 wt.% NaCl. a) Assemblage of multiple HAADF STEM images of film-metal structure; bright field (BF) STEM images of coarse outer (b) and finer inner (c,d) $Mg(OH)_2$. Cracks in structure are attributed to sample preparation (prep.).

Figure 7- DF STEM image of the film cross-section (a) and corresponding EDS elemental maps (b-e) for AZ31B after 24 h in D_2O with 5 wt.% NaCl

Figure 8- DF STEM images of the film cross-section formed on E717 after 24 h in H_2O with 5 wt.% NaCl (a,b) and D_2O with 5 wt.% NaCl (c).

Figure 9- DF STEM of the film cross-section (a) and corresponding EDS elemental maps (b-f) for E717 after 24 h in D_2O with 5 wt.% NaCl (same region as in Fig 7c).

Figure 10- DF STEM of the film cross-section (a) and corresponding EDS elemental maps (b-f) generated from the boxed region for AZ31B after 4 h in H_2O with 1 wt.% NaCl.

Figure 11- DF STEM DF of the film cross-section (a) and corresponding EDS elemental maps (b-f) generated from the boxed region for E717 after 4 h in H_2O with 1 wt.% NaCl.

Figure 12: Surface area distribution as a function of fitted feature radius size obtained from modeling the scattering data with a polydisperse hard sphere model.

Figure A1- Simplified schematic of a SANS experiment [after 40, 71].

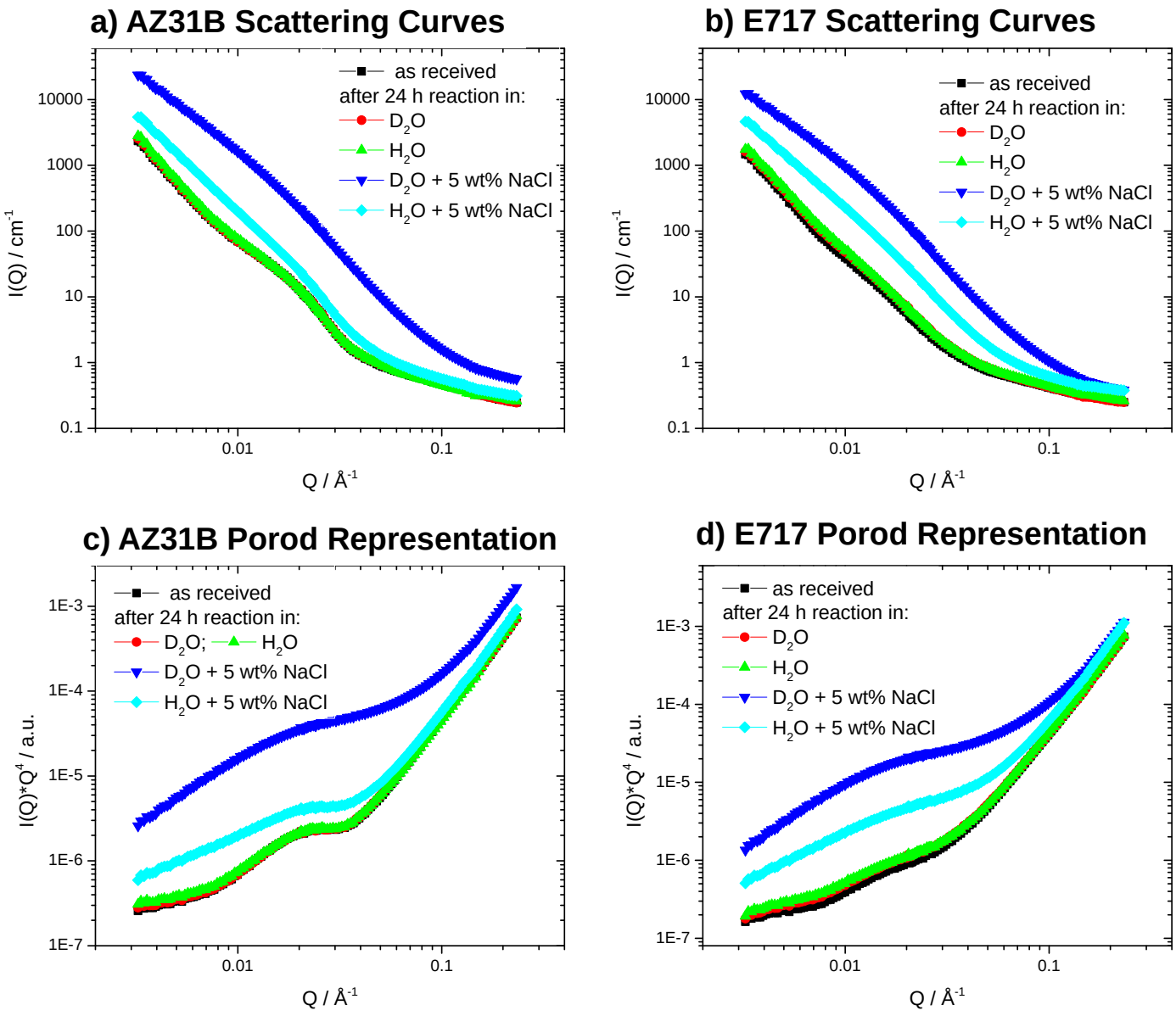

Figure 1-SANS scattering curves (a,b) and Porod representation (c,d) for AZ31B and E717. The black as-received, red 24 h D_2O, and green 24 h H_2O data points overlap considerably, such that they are not individually distinguishable in above plots.

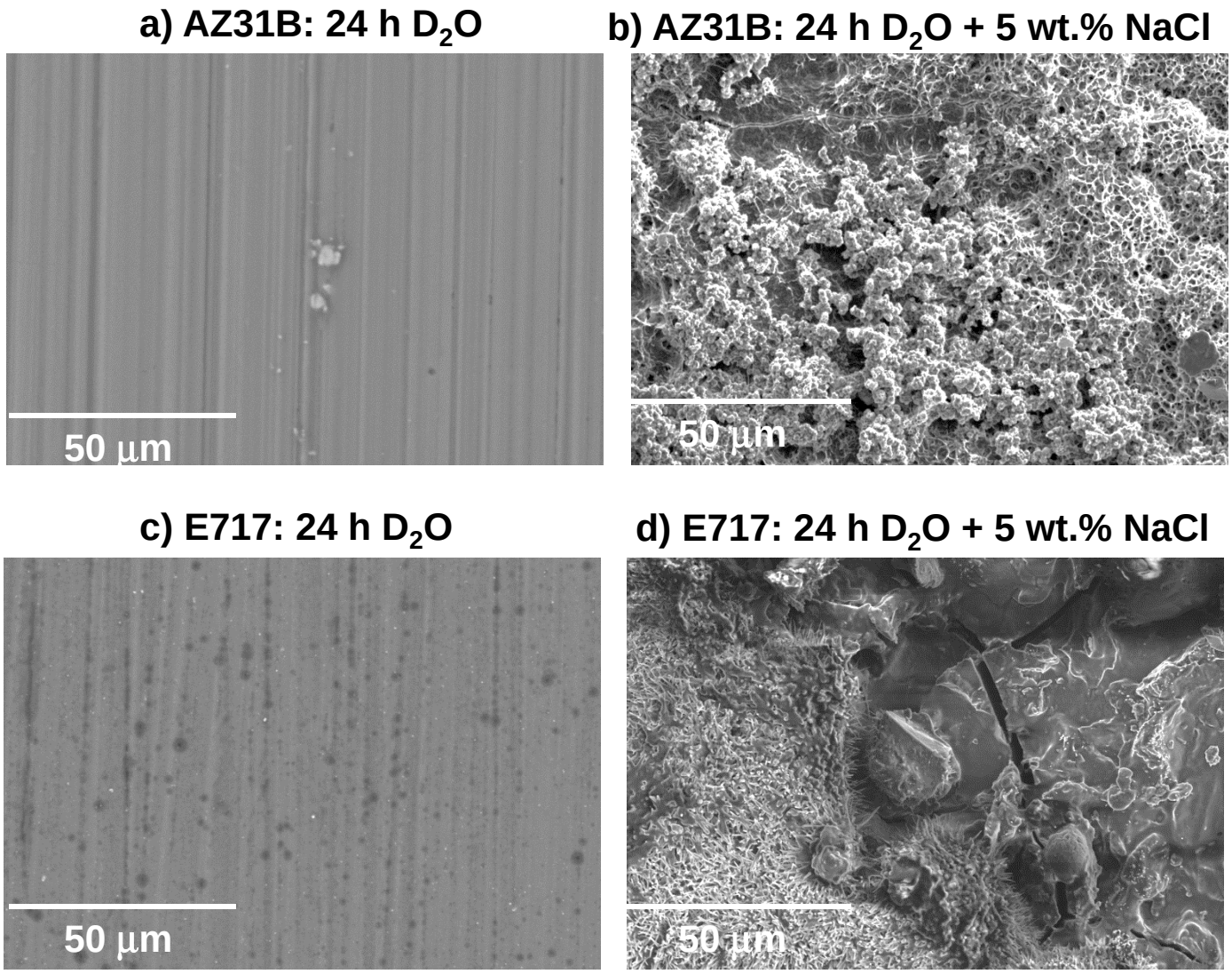

Figure 2- Surface SEM images of AZ31B and E717 after 24 h in D_2O (a,c) or 24 h in D_2O with 5 wt.% NaCl (b,d). Images (a,c) backscatter mode and images (b,d) secondary mode.

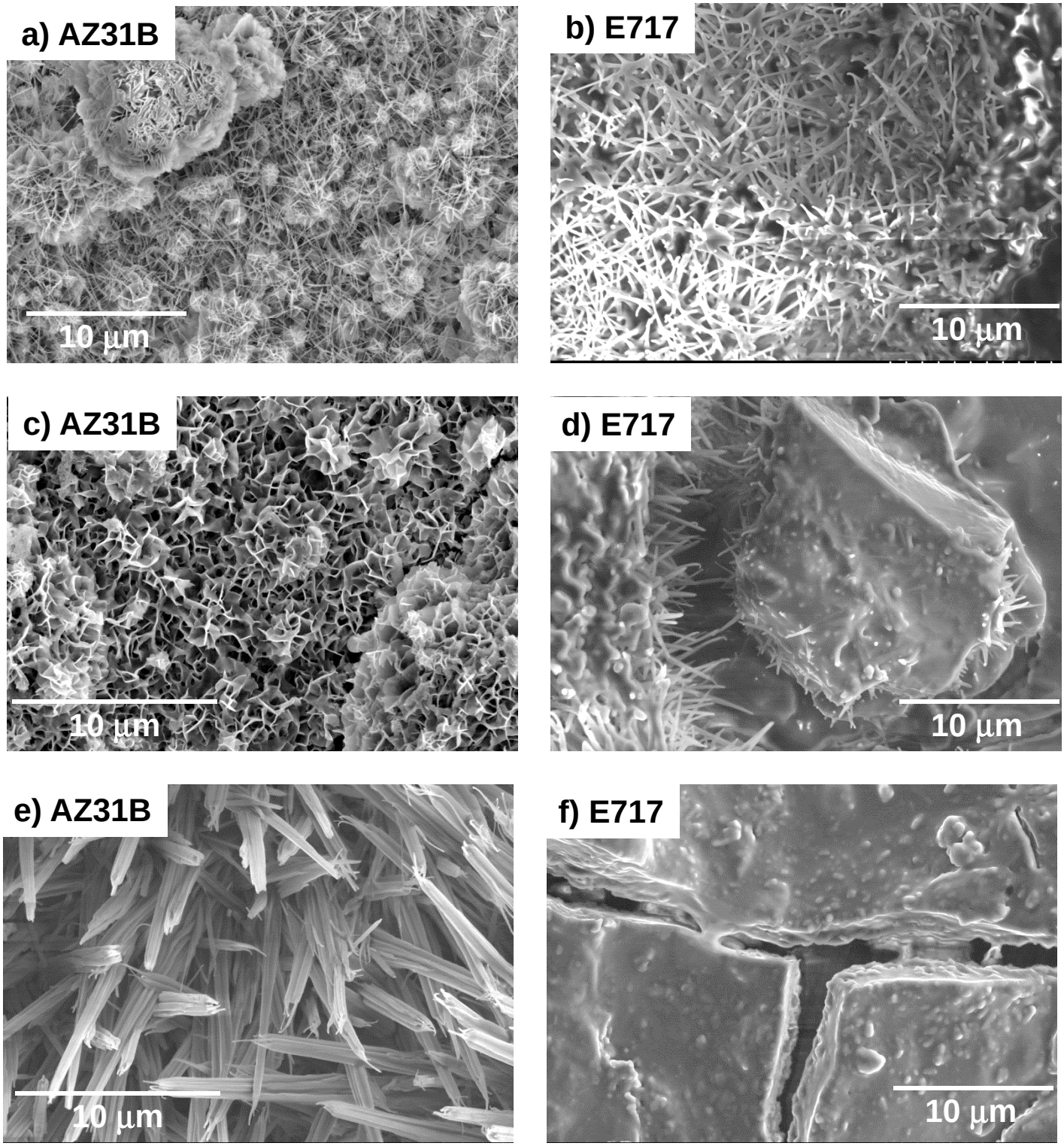

Figure 3- Surface secondary mode SEM images of AZ31B (a,c,e) and E717 (b,d,f) after 24 h in D_2O with 5 wt.% NaCl showing wide morphological variation of $Mg(OH)_2$ –base surface products formed.

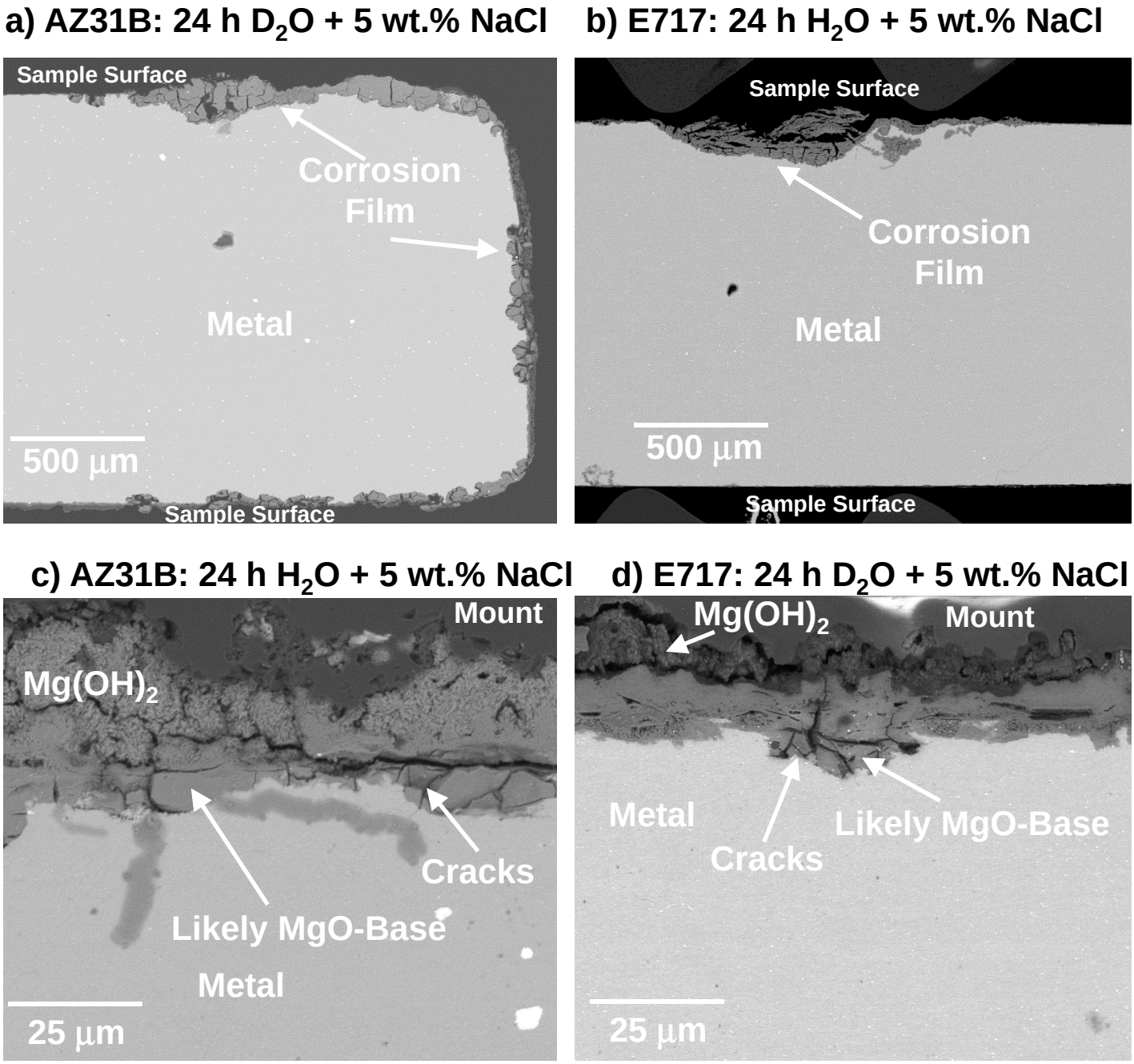

Figure 4- Cross-section backscatter mode SEM images of AZ31B and E717 after 24 h in D_2O or H_2O with 5 wt.% NaCl showing low magnification views illustrating non-uniform attack (a,b) and typical higher magnification images of retained scale regions (some outer film spallation during sample handling and preparation occurred).

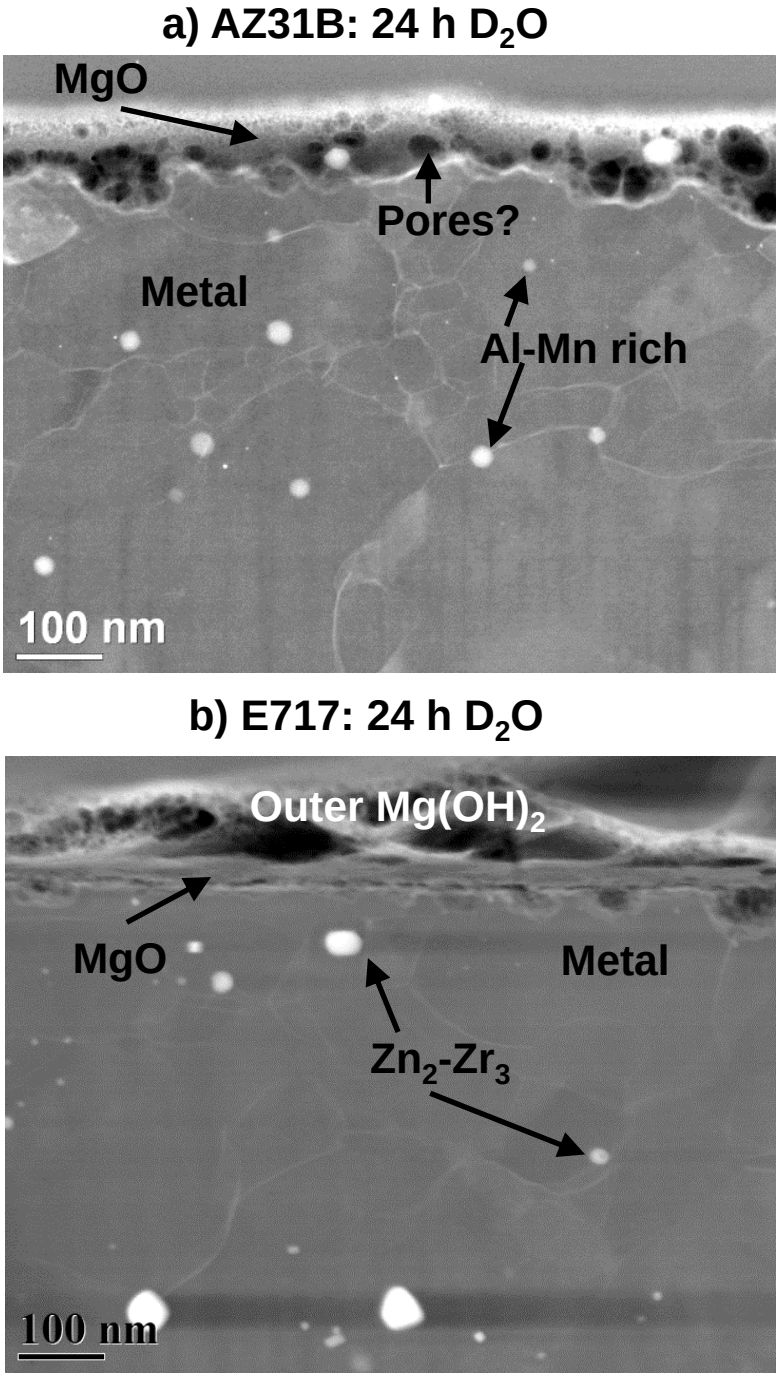

Figure 5- HAADF STEM images of film cross-sections formed on AZ31B (a) and E717 (b) after 24 h in D_2O.

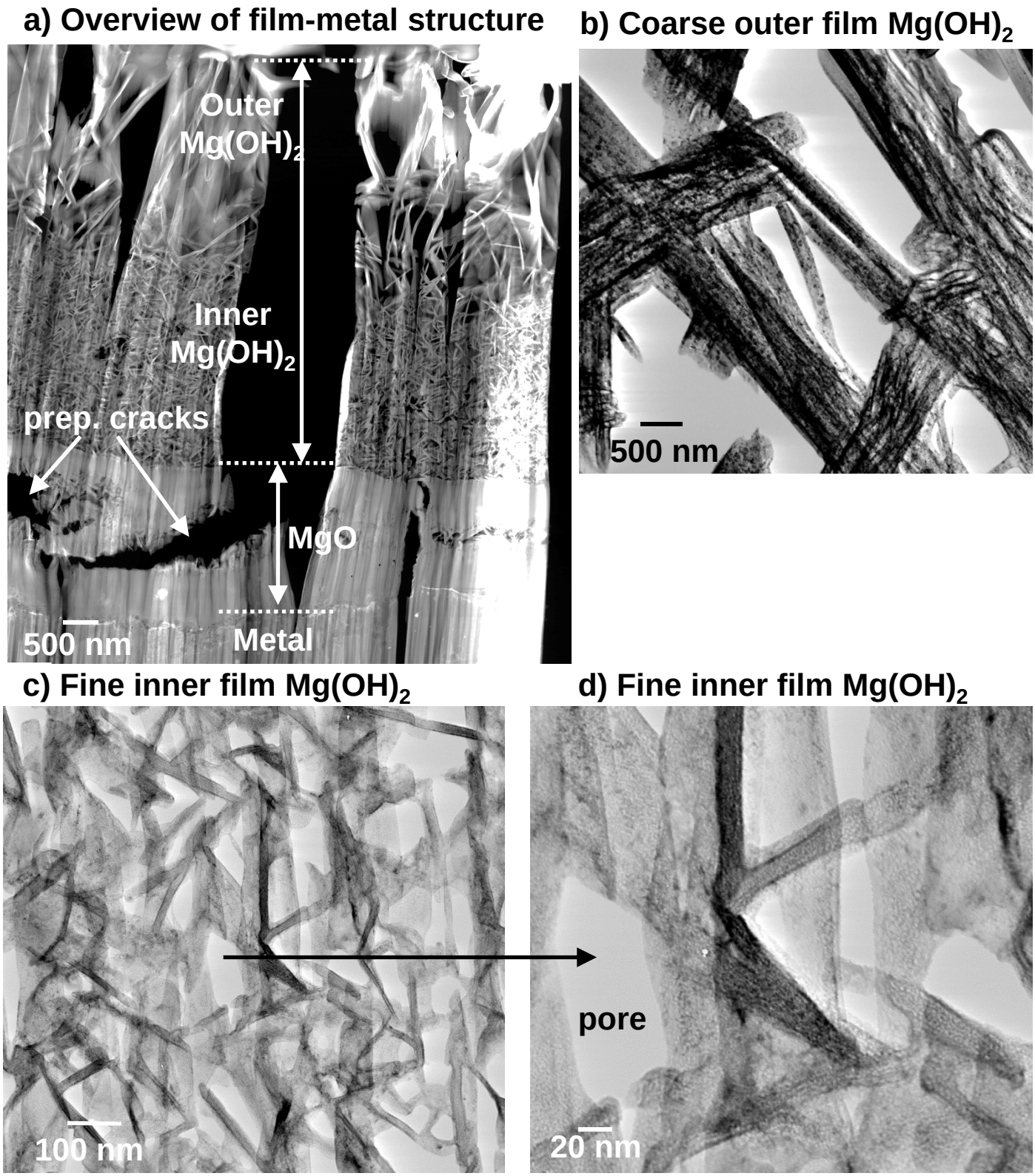

Figure 6- AZ31B after 24 h in D_2O with 5 wt.% NaCl. a) Assemblage of multiple HAADF STEM images of film-metal structure; bright field (BF) STEM images of coarse outer (b) and finer inner (c,d) $Mg(OH)_2$. Cracks in structure are attributed to sample preparation (prep.).

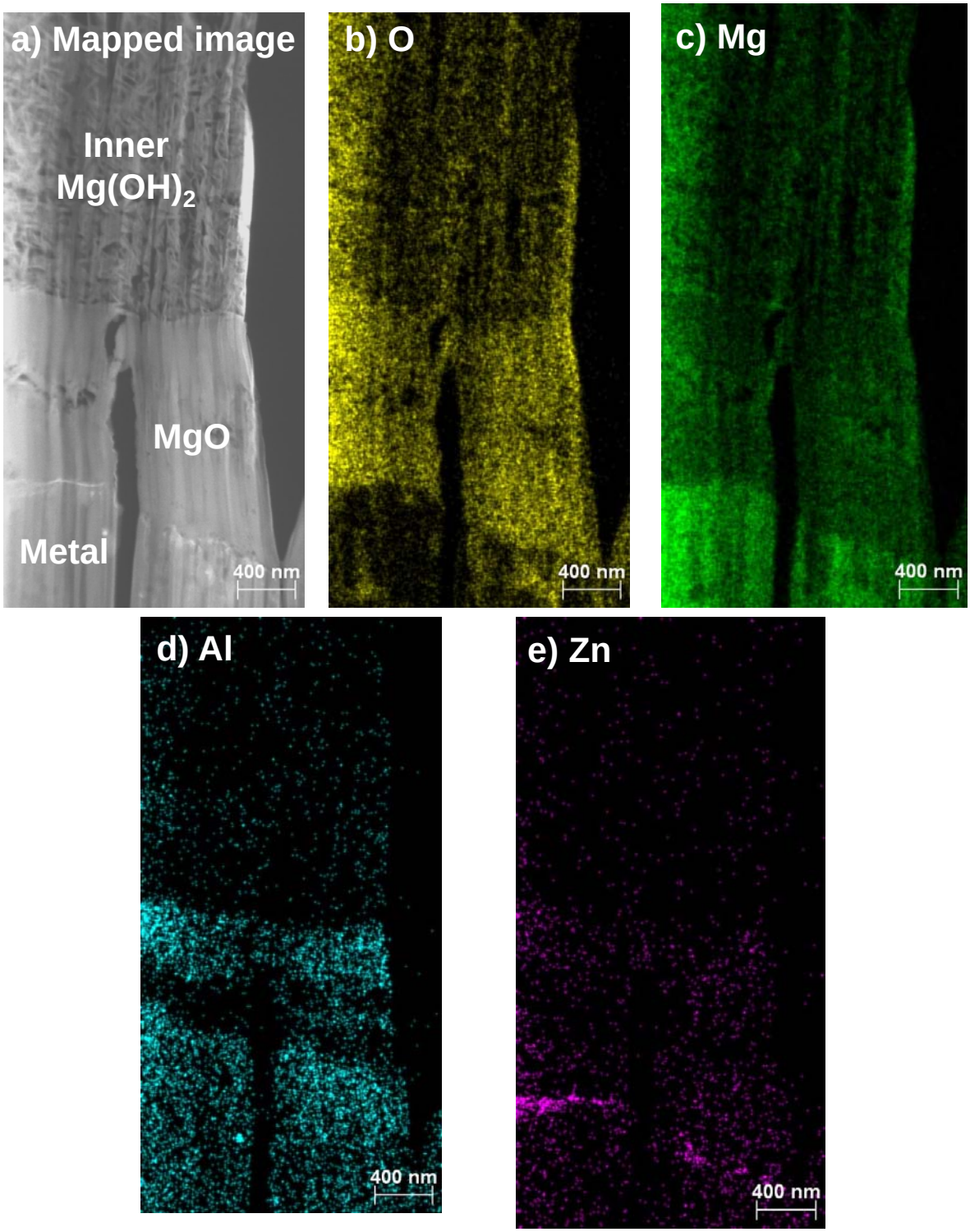

Figure 7- DF STEM image of the film cross-section (a) and corresponding EDS elemental maps (b-e) for AZ31B after 24 h in D_2O with 5 wt.% NaCl.

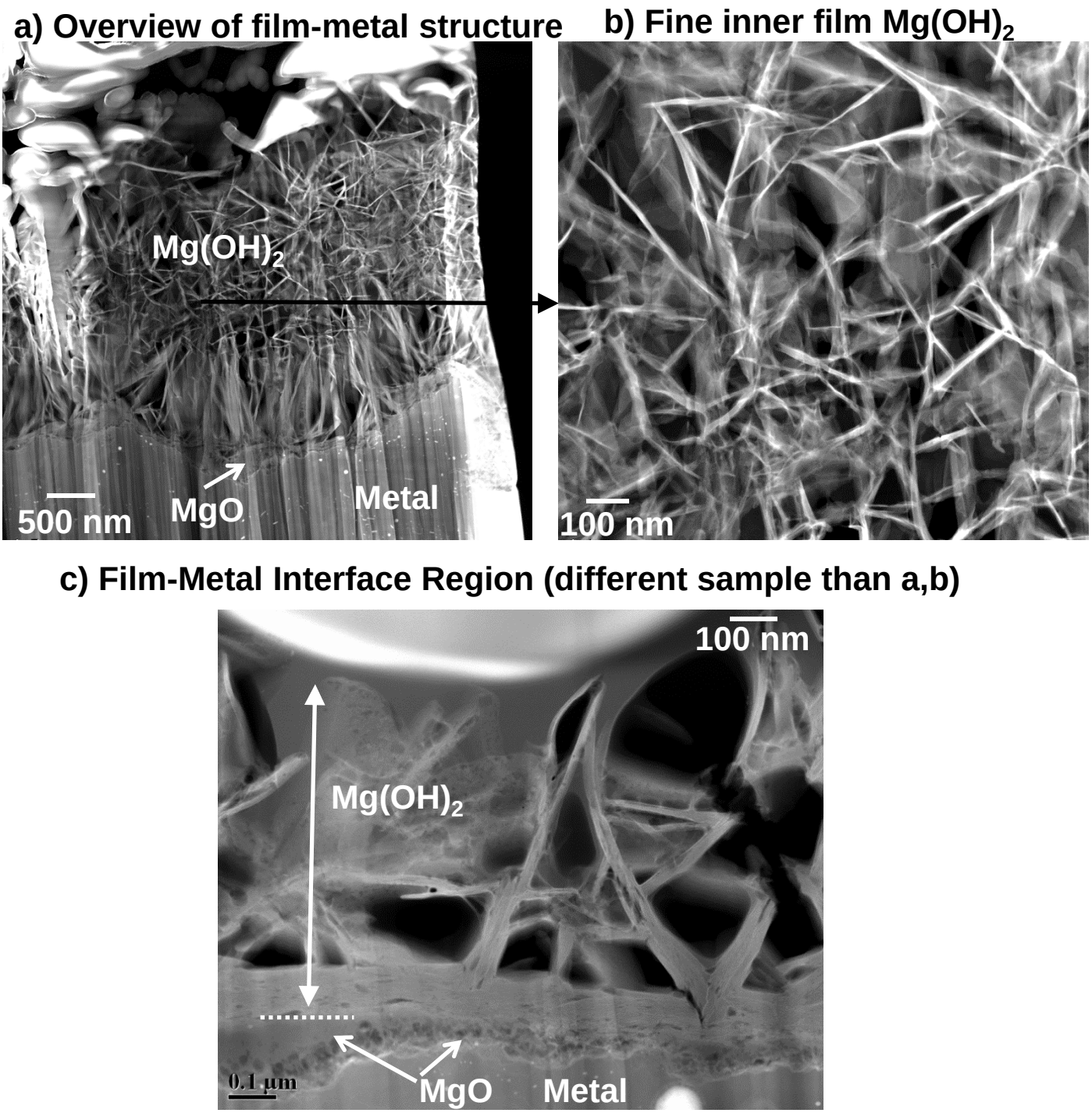

Figure 8- DF STEM images of the film cross-section formed on E717 after 24 h in H_2O with 5 wt.% NaCl (a,b) and D_2O with 5 wt.% NaCl (c).

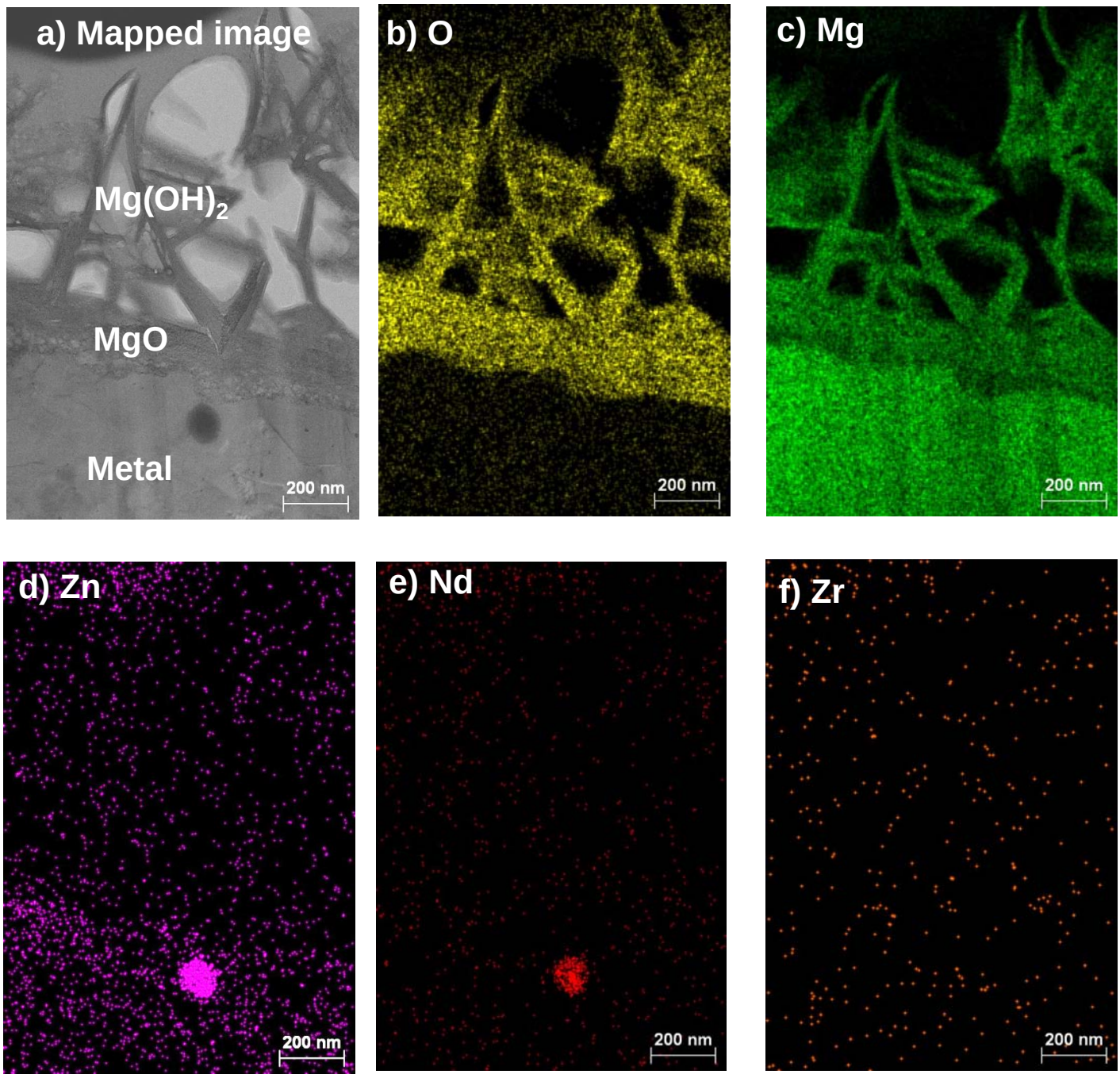

Figure 9- DF STEM of the film cross-section (a) and corresponding EDS elemental maps (b-f) for E717 after 24 h in D_2O with 5 wt.% NaCl (same region as in Fig 7c).

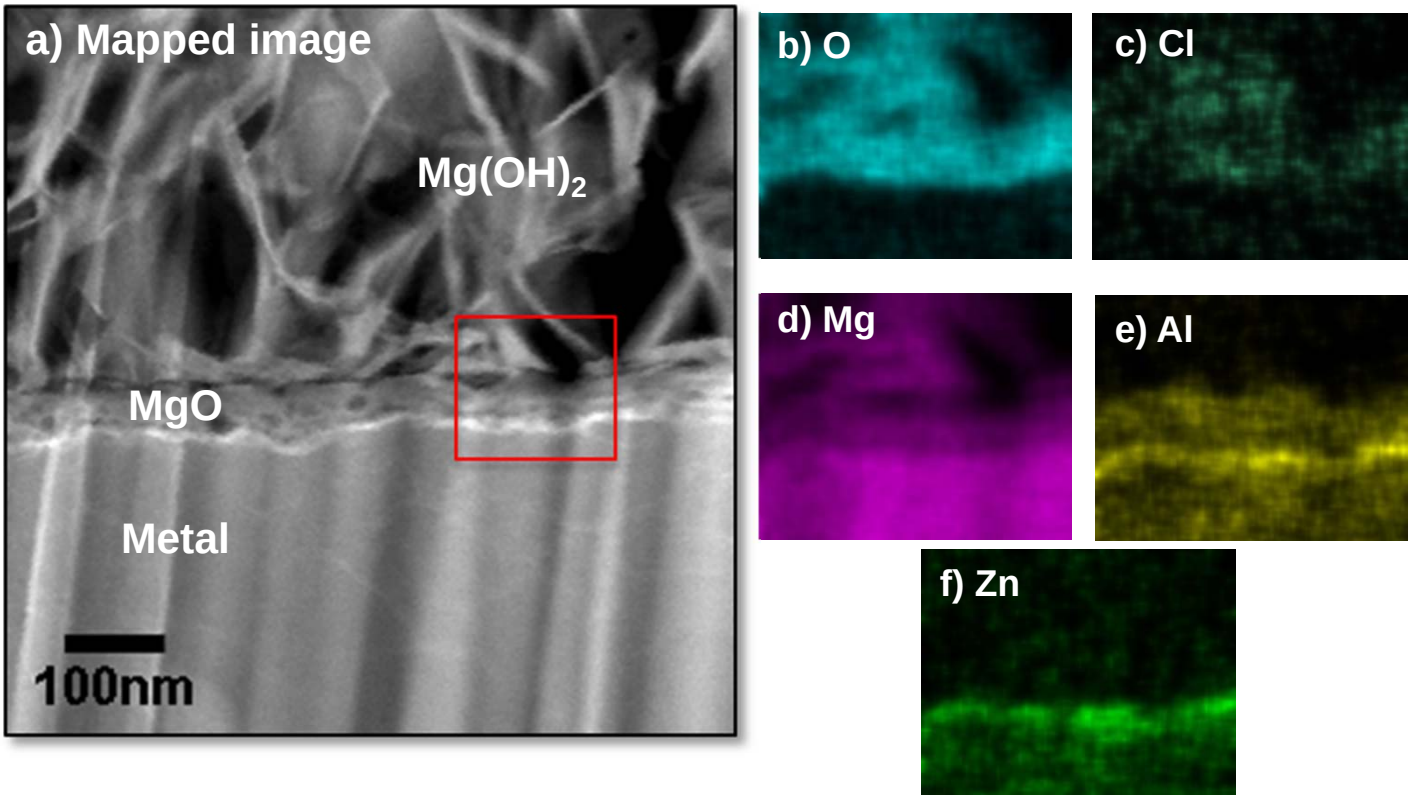

Figure 10- DF STEM of the film cross-section (a) and corresponding EDS elemental maps (b-f) generated from the boxed region for AZ31B after 4 h in H_2O with 1 wt.% NaCl.

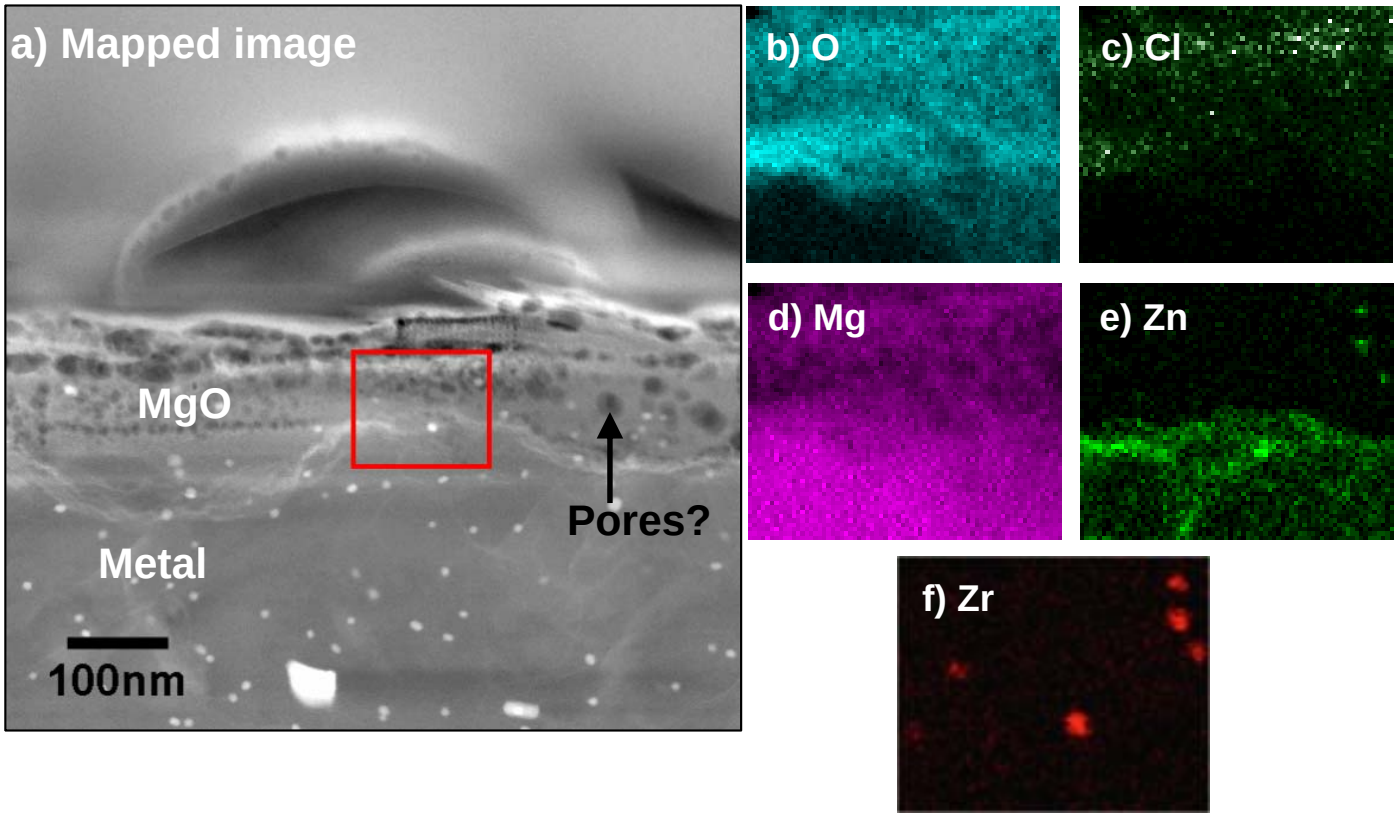

Figure 11- DF STEM DF of the film cross-section (a) and corresponding EDS elemental maps (b-f) generated from the boxed region for E717 after 4 h in H_2O with 1 wt.% NaCl.

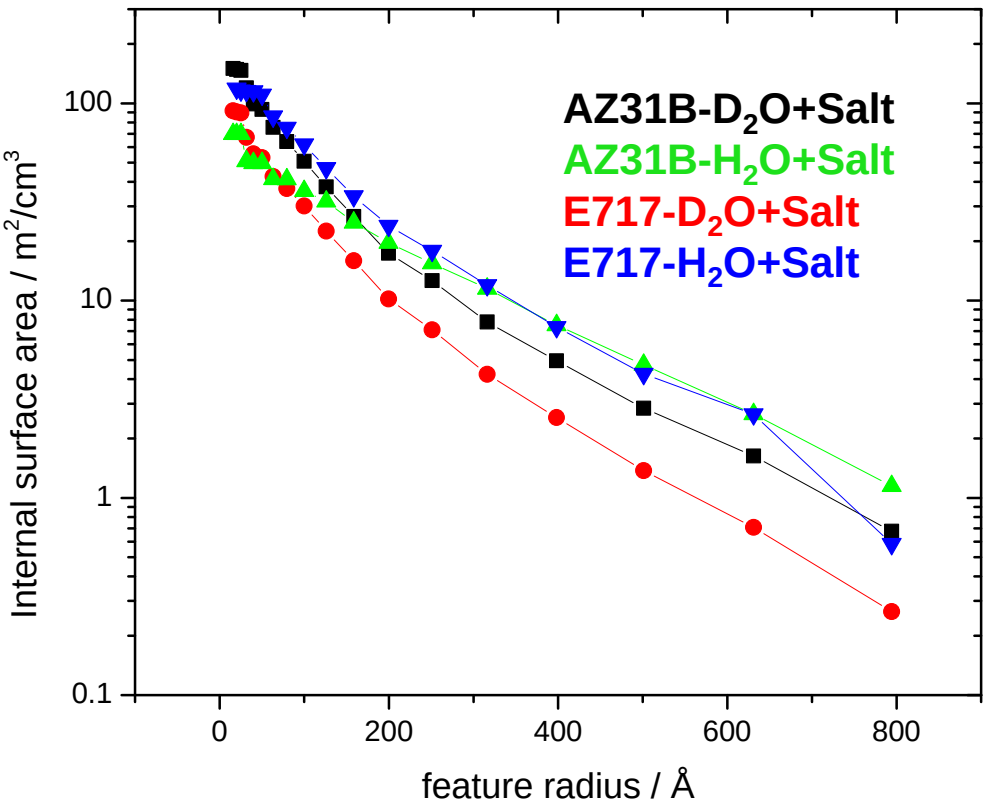

Figure 12: Surface area distribution as a function of fitted feature radius size obtained from modeling the scattering data with a polydisperse hard sphere model.

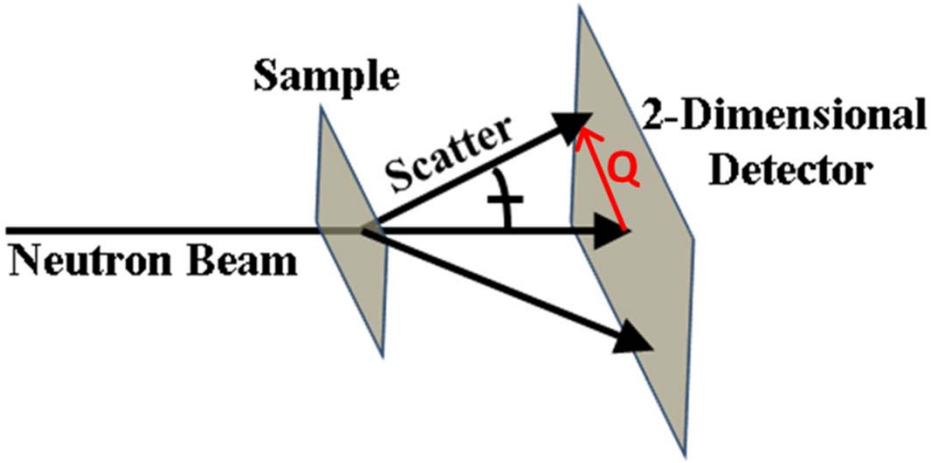

Figure A1- Simplified schematic of a SANS experiment [after 40, 71].